Luyang Geng[1]
Key Laboratory of Design and
Manufacture of Extreme Pressure Equipment,
School of Mechanical and Power Engineering,
Nanjing Tech University,
Nanjing 211816, China
e-mail: young@njtech.edu.cn

Shan-Tung Tu
Key Laboratory of Pressure Systems and
Safety (MOE),
School of Mechanical and Power Engineering,
East China University of
Science and Technology,
Shanghai 200237, China
e-mail: sttu@ecust.edu.cn

Jianming Gong
Key Laboratory of Design and
Manufacture of Extreme Pressure Equipment,
School of Mechanical and Power Engineering,
Nanjing Tech University,
Nanjing 211816, China
e-mail: gongjm@njtech.edu.cn

Wenchun Jiang
State Key Laboratory of Heavy Oil Processing,
College of Chemical Engineering,
China University of Petroleum (East China),
Qingdao 266580, China
e-mail: jiangwenchun@126.com

Wei Zhang
Key Laboratory of Design and
Manufacture of Extreme Pressure Equipment,
School of Mechanical and Power Engineering,
Nanjing Tech University,
Nanjing 211816, China
e-mail: hjzhw@njtech.edu.cn

On Residual Stress and Relief for an Ultra-Thick Cylinder Weld Joint Based on Mixed Hardening Model: Numerical and Experimental Studies

Residual stress distributions as welded and after local postwelding heat treatment (PWHT) of butted weld joint of a huge cylinder with ultra-thick wall were investigated by finite element (FE) simulations and measurement. Sequential coupling thermal-mechanical analyses were conducted with a generalized plane strain two-dimensional (2D) model to simulate the welding procedure bead by bead, combining with three-dimensional (3D) double-ellipsoid moving heat source and mixed isotropic–kinematic hardening plastic model. The simulation was validated by X-ray diffraction (XRD) measurements. Simulation results showed that local PWHT with heated band width of $0.5\sqrt{Rt}$ can significantly reduce the residual stress on the outer surface of weld joint, but bring about harmful high tensile stress on inner surface due to bending moment induced by local radial thermal distortion. For the purpose to find out the appropriate heated band width of local PWHT, relations between stress relief and size of heated band were studied. Results show that the stresses on the inner surface reach a maximum value when the heated band width is less than $1\sqrt{Rt}$. Based on the simulation results and from the view point of lowering the stress level on the inner surface, the optimum width of $3\sqrt{Rt}$ for heated band was proposed. [DOI: 10.1115/1.4040315]

Keywords: thick plate welding, weld residual stress, local PWHT, finite element method

1 Introduction

Multipass welding of pressure vessels and piping with thick wall will inevitably generate large welding residual stress (WRS) which is detrimental to the structural reliability [1]. The WRS would induce brittle fracture [2], reduce fatigue life [3,4], and lead to stress corrosion cracking (SCC) [5,6]. Furnace-based postwelding heat treatment (PWHT) is widely used as an effective method to reduce the harmful WRS for most weld joints. However, some weld joints such as pipe joints welded onsite or closure weld joints of huge vessels are not convenient to conduct furnace-based PWHT and the local PWHT is demanded.

In order to evaluate the effectiveness of PWHT on reducing harmful WRS, it is necessary to determine the distributions of WRS at the joint, especially on the inner surface of piping and vessels, where the joints contact with the medium and SCC occurs. However, the nun-destructive experimental methods used to measure WRS nowadays, including X-ray and Neutron diffraction techniques, have the shortcoming on the capacity of penetration, which makes it unlikely to measure the WRS of inner surface from outside while the inner space of pipe or vessel are

not big enough to place the test equipment. An alternative method is the finite element method (FEM), which was used to predict the WRS by Ueda [7] and Rybicki [8] first at the beginning of 1970s. During the followed years, significant progress has been made in welding simulation with FEM and resulted in the establishment of computational welding mechanics [9–11]. With the increasing computing power, FEM has been widely used to study the WRS and the effect of PWHT now. Song and Dong et al. [12–14] studied the WRS distribution of a P91 pipe with multilayer girth weld before and after uniform PWHT with two-dimensional (2D) FE model, and discussed the effect of important parameters of PWHT such as temperature, holding time, and component thickness. Gong and co-workers [15,16] predicted the WRS of P92 pipe with thick wall by three-dimensional FE model and studied the influence of heat source traveling speed and welding sequences on WRS. Mitra et al. [17] carried out bead-by-bead and lumped simulations of narrow-gap submerged arc welding (SAW) on 800 mm ultra-thick plate and investigated the effect of uniform PWHT, and found that the lumped models overpredicted the maximum as-welded residual stress and significant stress relief occurs in the first half hour of holding time during PWHT.

As for local PWHT for vessels and piping, there are several criteria over the world provide guidelines, such as ASME VIII, PD 5500, EN 13445, and the Chinese standard GB 150-2011. McEnerney and Dong [18] compared the difference among these criteria. Besides these criteria, a series researches were carried out by
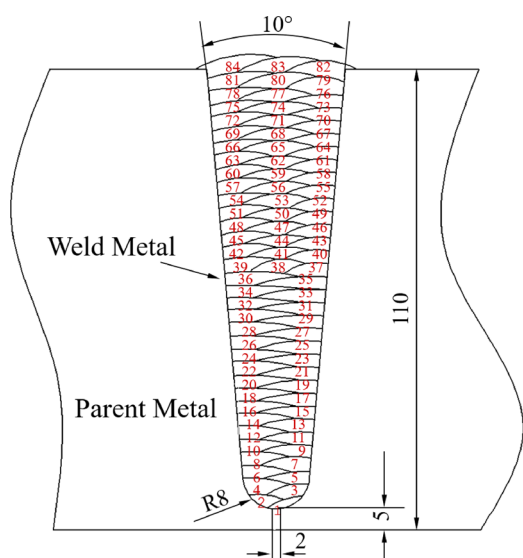

Table 1   Chemical compositions of 13MnNiMoR steel

C	Si	Mn	Cr	Ni	Mo	Nb	P	S
≤0.15	0.15–0.50	1.20–1.60	0.20–0.40	0.60–1.00	0.20–0.40	0.005–0.020	≤0.025	≤0.025
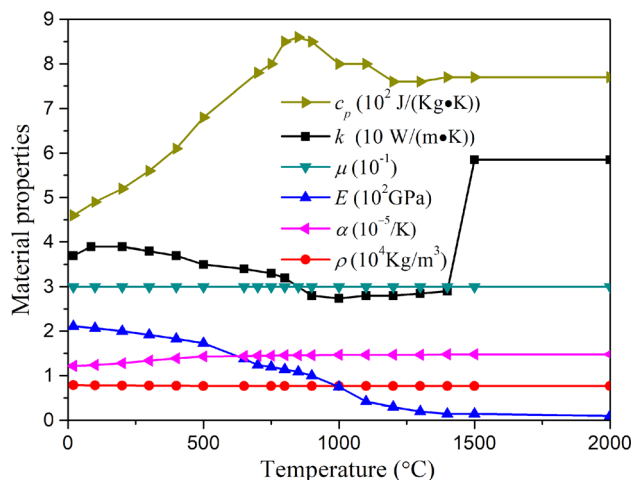
Fig. 1   Material properties for 13MnNiMoR steel

Fig. 2   Dimensional details of the single U groove and welding sequence

Wang et al. [19–21] to study the mechanical behavior in local PWHT on pipe girth weld with FEM and, as a result, a criterion of heated band width was proposed from the viewpoint of stress relief [22]. Nie and Dong [23] recommended a set of guidelines for defining the heated band width and location of local PWHT on different nozzle/vessel welds. As the local PWHT are often used for onsite applications like weld repairs, most of the research works presented focused on the pipe butted welding and nozzle/vessel welding. However, following the trend of large-scale

thickness of equipment in chemical, petrochemical, and power industries, the local PWHT are demanded but little attention has been paid on the effective of local PWHT on WRS.

In this paper, a generalized plane strain FE model of butted weld joint of huge cylinder with ultra-thick wall was developed with the commercial software program ABAQUS, according to the actual closure weld joint of an ethylene oxide reactor made in China with the largest diameter and wall thickness on the world. Bead-by-bead welding simulation and the local PWHT simulation were performed to determine the WRS distribution as welded and after the local PWHT, deploying double-ellipsoid moving heat source model, isotropic-kinematic mixed hardening material model, and Norton power creep law. Reliability of the simulation was validated by X-ray diffraction measurement. Furthermore, the formation mechanism of residual stress after local PWHT was discussed, and the influence of the circumferential heated band width on the WRS was studied to optimize the size of heated band.

2   Experimental

2.1   Material. The material of the cylinder is 13MnNiMoR, which is widely used as material for pressure vessels in China. The chemical compositions are listed in Table 1. The filler metal is $H_{08}Mn_2MoA/SJ107$, which is treated as the same material as 13MnNiMoR steel in FE analysis. The thermal–physical properties and mechanical properties dependent on temperature are shown in Fig. 1. These material properties, including specific heat capacity C_p, thermal conductivity k, coefficient of thermal expansion α, elastic modulus E, Poisson's ration μ, and the density ρ, are obtained from Ref. [24].

2.2   Welding Procedure. The butted weld joint was achieved by multipass welding including two stages: first, two root passes welding were carried out by shield metal arc welding, then the rest 82 passes were accomplished by SAW. Dimensional details of the single U groove and welding sequence is shown in Fig. 2. Before welding, the cylinders were placed on a saddle and preheated to a temperature of 200 °C. During the welding, the interpass temperature was between 200 and 300 °C. The welding parameters are shown in Table 2.

2.3   Local Postwelding Heat Treatment. Local PWHT was applied to the weld joint after it is cooled down to the room temperature. During the heat treatment, the weld joint was heated at outer surface by circumferential electric resistance heated bands with width of 300 mm, as shown in Fig. 3. The rest surface outside the heated band is protected by thermal insulated band in order to avoid excessive axial temperature gradients. The weld joint was first heated to 620 °C from room temperatures in 6–7 h with two steps, and then be held at 620 °C for 3 h before cooling down, as presented in Fig. 4.

2.4   X-ray Diffraction Measurement. Residual stress at five different locations on the outer surface of the joint were measured

Table 2   Welding parameters deployed for the weld joint

Welding type	Beads	Welding current (A)	Voltage (V)	Welding speed (mm/min)	Electrode diameter (mm)
Shield metal arc welding	1–2	160	22	150–210	3.0
SAW	3–81	700	30	410–420	3.5
SAW	82–84	750	34	420–430	3.5
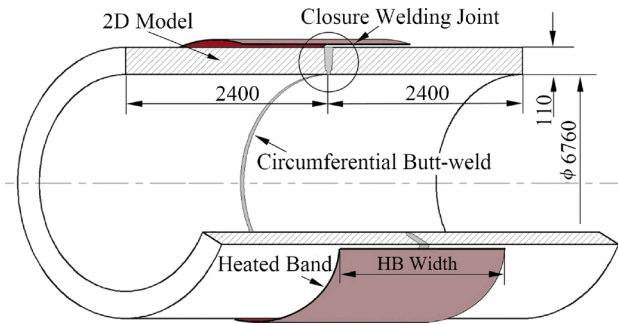
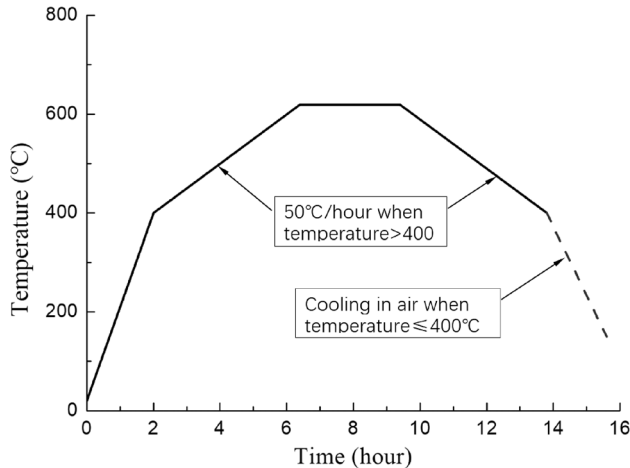**Fig. 3 Dimensional details of the cylinder and 2D FE model**

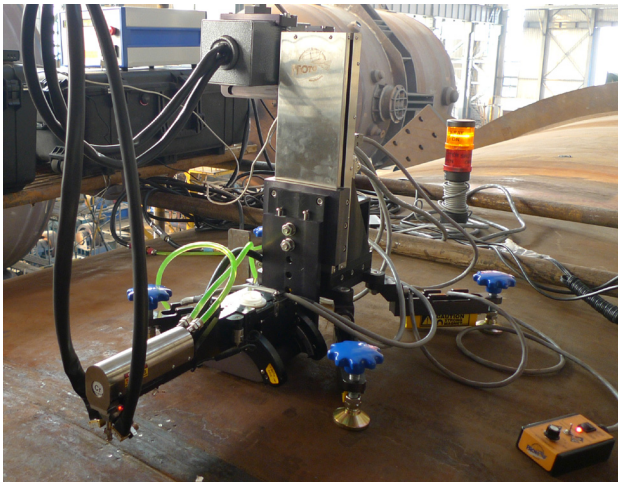**Fig. 4 Thermal cycle of the local PWHT**

Fig. 5 Setup of residual stress measurement by portable X-ray equipment on site

onsite with a portable X-ray equipment IXRD Combo, developed by Proto Manufacturing Limited, Oldcastle, ON, Canada, as shown in Fig. 5. The surfaces of these locations, including center of weldment, heat affected zone (HAZ), and parent metal, were electropolished to remove the oxide layer of the metal before the measurement, as shown in Fig. 6. In the measurements, Cr_K-Alpha was employed as radiation, Ferritic{211} was chosen as the measured crystal face, the operating voltage was 20 KV, the working current was 4 mA, wavelength was 2.291 Å, exposure time was 1 s, number of exposure was 10 times, and aperture was 1 mm.

Fig. 6 Locations of WRS measurement

3 Welding Simulation

3.1 Finite Element Model. A generalized plane strain 2D FE model of cylinder, with inner diameter of 6760 mm, wall thickness of 110 mm and length of 4800 mm, was built. The dimensional details of the model are shown in Fig. 3. Considering the influence of rest parts of the vessel, rotation constraints were applied at the both ends of the model. Axial displacement of the right end was constrained to avoid rigid body displacement. The ambient temperature was 20 °C. Both the outer surface and inner surface had the same convection coefficient of 8 W/(m² K) and radiation emissivity of 0.85, and the parameters of the surface protected by thermal insulated band were 8×10^{-7} W/(m²K) and 0.0005, respectively.

To simulate the thermo-mechanical behavior of material during welding process, a sequential coupling analysis was conducted. This analysis was divided into two parts: first, a heat conduction analysis was carried out to obtain the temperature distribution throughout the welding process and then followed by a mechanical analysis based on the thermal analysis results to compute the WRS and deformation.

Both the thermal analysis and mechanical analysis employed the same finite element meshes as shown in Fig. 7. The meshes were refined enough at the filler metal and vicinities to get satisfied accuracy. Element types DC2D4 and CPEG4 were used for thermal analysis and mechanical analysis, respectively. The process of passes filling was simulated by the element remove and add method, which removed all the elements of filler metal at first and then reactivated them bead by bead according to the actual welding sequence shown in Fig. 2.

3.2 Thermal Analysis. In thermal analysis, double-ellipsoid moving heat source model, proposed by Goldak et al. [25], was used to define the power density distribution in the moving welding pool. This volumetric heat source model is composed of the front and rear half parts, as shown in Fig. 8. In order to
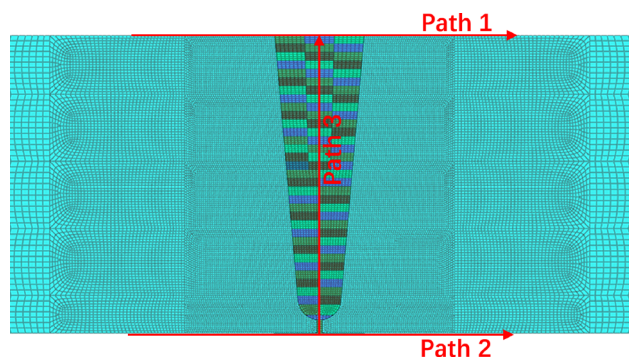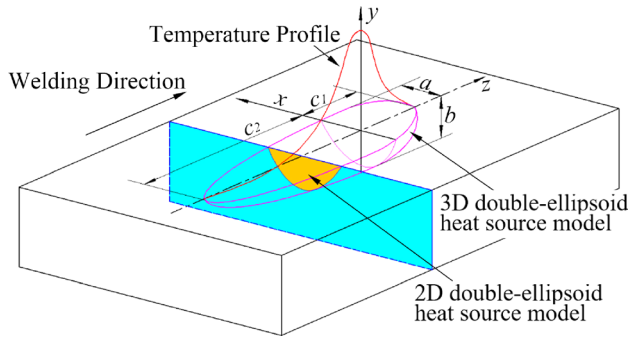

Fig. 7 Finite element meshing of the weld joint

Fig. 8 Double-ellipsoid heat source incorporated into a 2D FE model

incorporate this three-dimensional (3D) heat source model into a 2D FE model, it is assumed that the 3D heat source moves across a plane, the 2D model, with a speed v. The power density distribution in the heat source is defined by a Goldak equation, which is expressed in following form:

For the front half heat source:

$$q(x, y, t) = \frac{6\sqrt{3}Qf_1}{abc_1\pi\sqrt{\pi}} e^{\left[-\frac{3x^2}{a^2} - \frac{3y^2}{b^2} - \frac{3z^2}{c_1^2}\right]} \quad (1)$$

and for the rear half heat source

$$q(x, y, t) = \frac{6\sqrt{3}Qf_2}{abc_2\pi\sqrt{\pi}} e^{\left[-\frac{3x^2}{a^2} - \frac{3y^2}{b^2} - \frac{3z^2}{c_2^2}\right]} \quad (2)$$

where x and y are the local coordinates in the heat source, and $z = c_1 - vt$ defines the distance between the plane and the center of heat source. The total net heat input, Q, is calculated by equation $Q = \eta UI$, where U is arc voltage, I is welding current, and η is the arc efficiency factor, which was assumed to be 0.75 in this study according to Ref. [26]. The dimensions of heat source are defined by a, b, c_1, and c_2, as shown in Fig. 8. The front and rear parts of the heat source share the energy Q by the fraction factors f_1 and f_2, the sum of which are set up to be 2. In this study, f_1 was 1.4 while f_2 was 0.6, which means the major heat deposit in the front part of heat source. This heat source was deployed in the thermal analysis by a user subroutine DFLUX compiled by Fortran code.

For the purpose of obtaining appropriate values of the parameters a, b, c_1, and c_2, a 2D heat conduction FE analysis was carried out at first to simulate the welding process of a plate specimen with a double U groove, which was welded with the same welding parameters as the cylinder. The parameters a, b, c_1, and c_2 were calibrated by fitting the predicted fusion zone with the macrograph of the plate specimen, which is shown in Fig. 9. The fusion zone is assumed to be the material experienced a temperature at or above 1480 °C, the melting temperature of 13MnNiMoR steel. Furthermore, from Fig. 9, it is easy to see that the region at temperatures between 970 °C and 1480 °C agrees with the coarse grain heat affected zone, and the fine grain heat-affected zone. 970 °C is the normalizing temperature of 13MnNiMoR steel. The intercritical heat-affected zone was set to experience temperature above 715 °C, which is the phase-transition temperature AC_1. The parameters a, b, c_1, and c_2 are listed in Table 3.

3.3 Mechanical Analysis. Due to the thermal cycles experienced in multipass welding, the following mechanical analysis took account of plastic behavior of material under cycle load via isotropic–kinematic mixed hardening model. As shown in Fig. 10, due to the cycle load, the yield surface of material will contract/expand in stress space and translate simultaneously—the latter is known as Bauschinger effect. The proof stress σ_p at the same
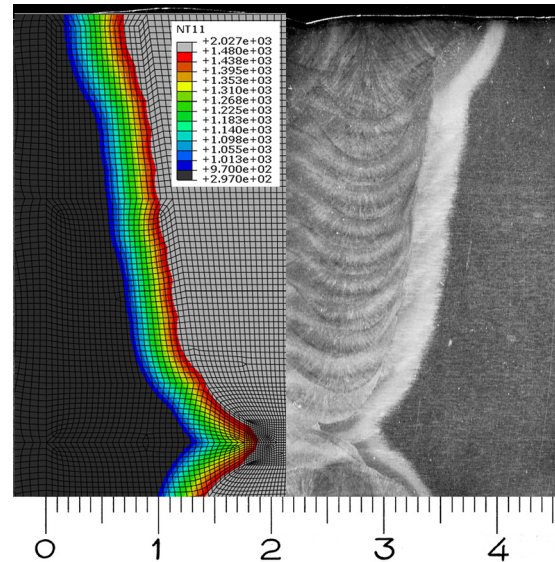
Fig. 9 Predicted fusion zone, coarse grain HAZ, and fine grain HAZ compared with the macrograph of joint

Table 3 Dimension parameters of the heat source

Bead pass	a (mm)	b (mm)	c_1 (mm)	c_2 (mm)
1–2	6	8	6	12
3–81	14	15	14	28
82–84	16	18	16	30
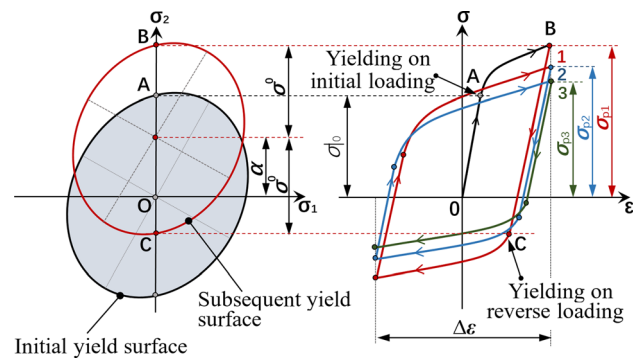
Fig. 10 Yield surface contract/expand and translate simultaneously due to cycle load

strain will increase or decrease as the number of cycles increase. The mixed hardening model describes both the expanding/contracting and translating of the yield surface, and is proved to predict the WRS with satisfactory accuracy [27–29].

Mixed hardening model was deployed in mechanical analysis via a Lemaitre–Chaboche formulation, which consists of two components defining the cyclic hardening/softening and Bauschinger effect, respectively. The isotropic hardening component, assuming the radius of the yield surface, σ^0, evolving with equivalent plastic strain $\bar{\varepsilon}^{pl}$, is expressed as

$$\sigma^0 = \sigma_{|0} + Q_{inf}(1 - e^{-b\bar{\varepsilon}^{pl}}) \quad (3)$$

where $\sigma_{|0}$ is the yield stress at zero plastic strain, and Q_{inf} and b are temperature-dependent material parameters. The kinematic hardening component describes the translation of the yield surface by defining the hardening rate of back stress tensor $\dot{\alpha}$, as function of equivalent plastic strain rate $\dot{\bar{\varepsilon}}^{pl}$ in the following form:

$$\dot{\alpha} = \sum_i \left[C_i \frac{1}{\sigma^0} (\sigma - \alpha) \dot{\bar{\varepsilon}}^{\mathrm{pl}} - \gamma_i \alpha_i \dot{\bar{\varepsilon}}^{\mathrm{pl}} \right] \tag{4}$$

where C_i and γ_i are temperature-dependent material parameters; σ is the applied stress tensor, and σ^0 is the radius of yield surface defined in Eq. (3). The σ^0, $\sigma_{|0}$, and α are described in Fig. 10.

The temperature-dependent material constants $\sigma_{|0}$, $Q_{\inf}$, b, C_i and, γ_i for 13MnNiMoR steel used in this study were obtained by fitting the results of uniaxial cyclic tests under strain control with total strain range $\Delta\varepsilon = 1.6\%$. The experiment temperatures ranged from $20\,^{\circ}\mathrm{C}$ to $800\,^{\circ}\mathrm{C}$. The cyclic softening curves of 13MnNi-MoR steel by experiments, which illustrate how the proof stress σ_p at the max strain 0.8% decreases with the number of cycles, are compared in Fig. 12 with those predicted by 3D FE simulations (as shown in Fig. 11) via the mix hardening model and acquired material constants. These curves indicate that the 13MnNiMoR steel subject to cyclic softening effect at all the temperatures, which will affect the accuracy of WRS prediction. The material constants for 13MnNiMoR steel are listed in Table 4.

4 Local Postwelding Heat Treatment Simulation

To investigate the effect of the local PWHT on WRS distribution, the local PWHT simulations were conducted as subsequent procedure of welding simulation. Same as the welding simulation, the local PWHT simulation deployed sequential coupling analysis too. In the thermal analysis, thermal cycle shown in Fig. 4 was applied to heated zone of the FE model. During the mechanical analysis, the distribution of stress and other variables obtained in welding simulation, such as back stress tensor and equivalent plastic strain, were set as initial condition. Norton's steady-state creep model is used to predict the stress relief during the PWHT
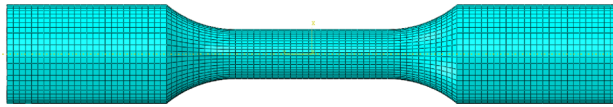

Fig. 11 Three-dimensional FE model of the specimen under uniaxial cycle load
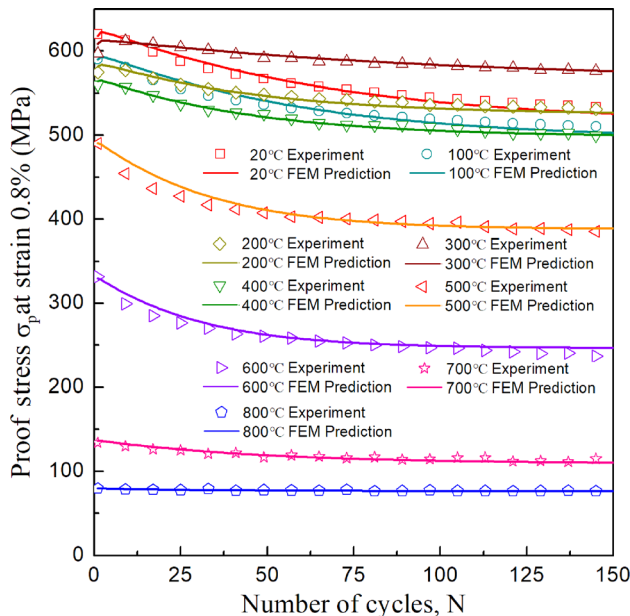

Fig. 12 Cyclic softening curves at different temperatures obtained by experiments and FE simulation

Table 4 Mixed hardening model parameters of 13MnNiMoR steel

Temperature (°C)	$\sigma_{|0}$ (MPa)	$Q_{\inf}$	b	C_1	γ_1	C_2	γ_2
20	416	−128.78	0.823	79,958	690	22,648	18.08
100	387	−118.91	0.819	79,871	743	23,755	17.63
200	383	−72.74	0.789	88,610	891	24,153	17.19
300	381	−63.93	0.601	121,816	1005	28,242	17.02
400	376	−78.37	1.238	121,674	1054	17,763	14.02
500	365	−113.48	1.482	81,810	1014	10,564	11.05
600	235	−90.12	1.526	62,465	998	6619	10.44
700	90	−27.58	1.052	26,418	723	2006	9.2
800	58	−3.18	1.210	16,104	1083	988	5.2

$$\dot{\varepsilon} = A\sigma^n \tag{5}$$

where $\dot{\varepsilon}$ is the rate of creep strain, σ is the uniaxial stress, and A and n are temperature-dependent material constants. The values $A = 3.44 \times 10^{-17}$, $n = 4.54$ at $420\,^{\circ}\mathrm{C}$ and $A = 1.8 \times 10^{-15}$, $n = 4.54$ at $600\,^{\circ}\mathrm{C}$ were employed in simulation.

5 Finite Element Method Validation

In order to validate the results of welding and PWHT simulation, the residue stress distribution of outer surface predicted by FE simulations was compared to the results of X-ray diffraction (XRD) measurements. Due to the shape limit of the cylinder, only the hoop stress was convenient to be measured on site, as shown in Fig. 5. Figure 13 compares the hoop stress predicted by simulation and XRD measurements along axial reference Path1 on outer surface as shown in Fig. 7. It's evident that the results of simulation fit well to the measured data except at the center of weld, which indicates that the material behavior of filler metal is different from that of parent metal. It should be noted that the distance between the observed fusion lines on outer surface is wider than prediction due to the melted filler metal overflows the groove, but it does not obviously affect the prediction accuracy of stress adjacent to the lines.

6 Results and Discussion

6.1 As-Welded Residual Stress. The welding residual stress is mainly induced by the nonuniform temperature field that exists in weld joint and vicinities during welding. As for weld joint with thick wall, the temperature field will be more complicated due to thermal cycles experienced during the multipass welding.
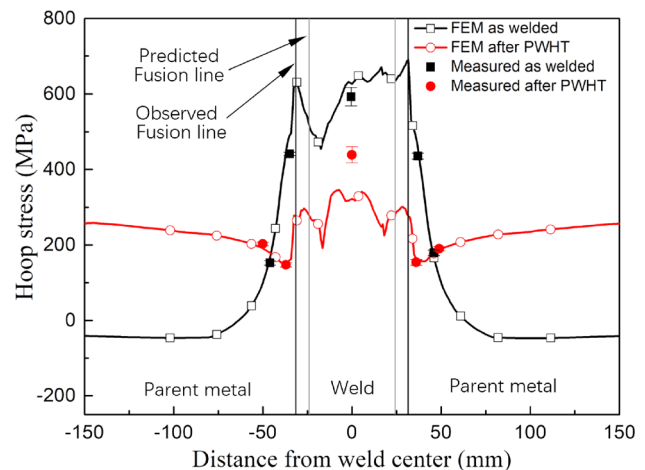

Fig. 13 Comparison of hoop stress distribution between simulation and measurements on outer surface
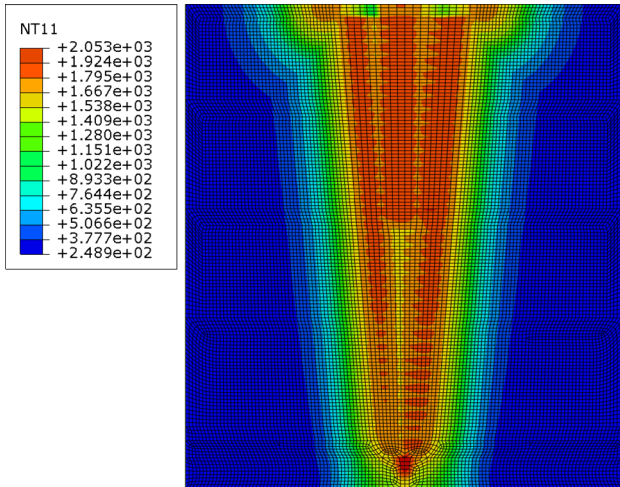
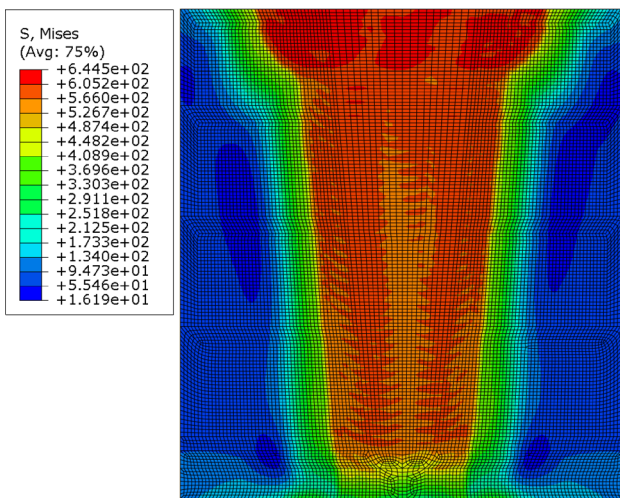**Fig. 14 Contour of the highest temperature experienced during welding**

Fig. 15 Contour of the residual Mises stress within weld joint

Figure 14 shows the contour of the highest temperature experienced by the material during welding, and Fig. 15 shows the distribution of Mises stress in weld joint. It is clear that the complicated temperature field inevitably lead to the complicated stress distribution. From Fig. 15, it can be found that the stress level of weld and HAZ is much higher than that in parent metal, and the stress level on the outer surface of weld is higher than that of inner surface. The maximum Mises stress with value of 645 MPa occurs at the outer surface, where the last weld bead deposit, while the value of 16 MPa emerged at parent metal not far away from the weld, and the inner surface of weld, where the first weld bead deposit, show a Mises stress value of 311 MPa.

The distributions of as-welded radial, axial, and hoop stresses are analyzed in detail along three reference paths represented in Fig. 6, including the axial Path1 on outer surface, axial Path2 on the inner surface and radial Path3 at the center of weld from inner surface to outer surface.

Figure 16 shows the stress distributions along the axial reference Path1 on the outer surface. It is clear that the hoop stress is of high level tensile stress at filler metal zone and HAZ on the outer surface, and achieves the maximum value of 690 MPa at the boundary of HAZ. Next to this location, the hoop stress reduces sharply and is opposite with compressive stress at parent metal. Within the filler metal zone, the hoop stress decreases at the center of weld beads, especially at the last bead. The axial stress reaches
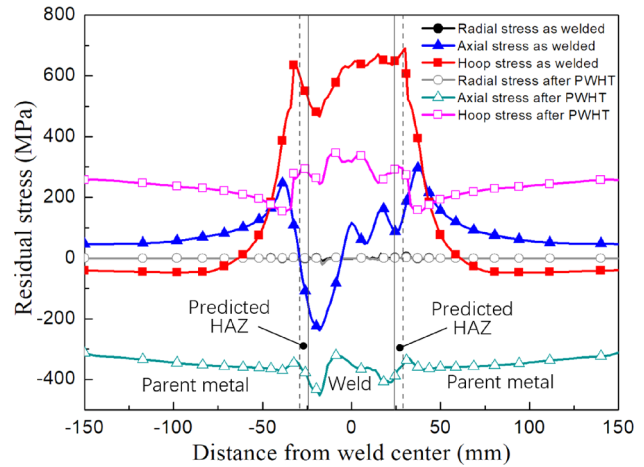

Fig. 16 Distribution of residual stress along axial Path1 on outer surface

the highest value of 296 MPa at parent metal adjacent to HAZ and reduces relatively more smoothly than hoop stress to a low value above zero in parent metal. Similar to hoop stress, the axial stress decreases within weld beads, but is opposite with high compressive stress of −261 MPa at the center of the last bead. The radial stress is almost zero and only fluctuates slightly at filler metal zone.

Figure 17 display the distributions of stress along axial Path2 on the inner surface. It's obvious that the stresses have the same tendency as those along Path1 on outer surface. The hoop stress reaches the highest value of 416 MPa at the boundary of HAZ, which is significantly lower than the counterpart on the outer surface, while the axial stress has a maximum value of 301 MPa, almost the same value on the outer surface. Both hoop and axial stresses reduce to compressive stress at parent metal away from the HAZ. At the center of the weld where the initial bead deposits, the axial stress decreases sharply to compressive stress while the hoop stress keeps tensile. The radial stress on the inner surface is as tiny as that on the outer surface.

The distribution of stress on the radial Path3 at the center of weld from inner surface to the outer is shown in Fig. 18, from which it is clearly seen that the hoop stress is tensile through the whole wall thickness and the value on the inner surface are obviously less than that on the outer surface. The hoop stress increases quickly from 259 MPa on inner surface to the maximum value of 658 MPa at 15% thickness from inner surface and then gradually
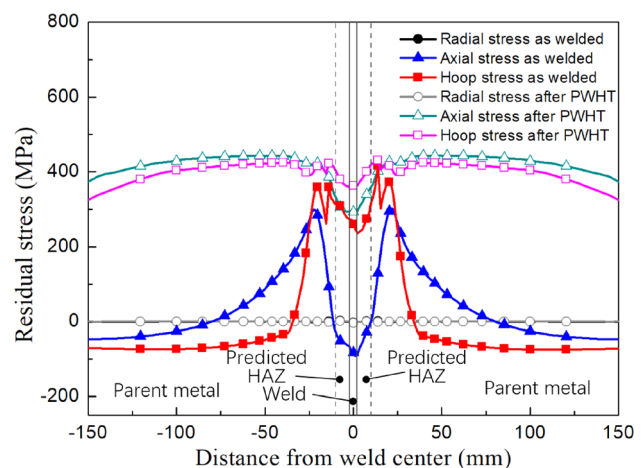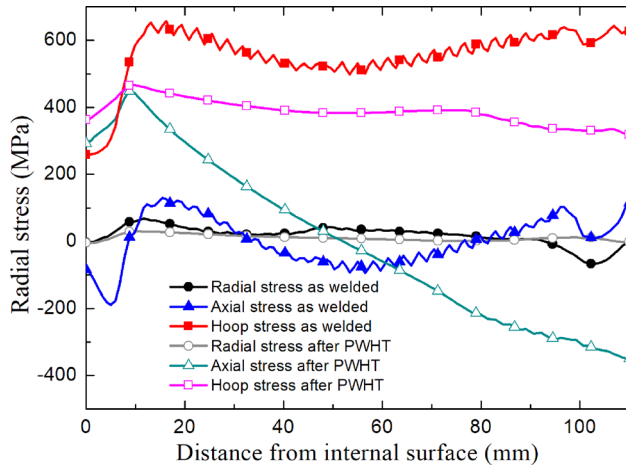

Fig. 17 Distribution of residual stress along axial Path2 on inner surface

Transactions of the ASME

Fig. 18 Distribution of residual stress along radial Path3 at the weld center from inner surface to outer surface

reduces to 502 MPa at the middle wall and at last reaches a relative high value of 626 MPa on the outer surface. The distribution of axial stress shares the same shape with hoop stress at lower strength level, representing compressive stress at the inner surface and middle thickness. Contrast to the hoop and axial stresses, the radial stress is smaller and changes more smoothly along Path3. Figure 18 shows that the distribution profiles of hoop and axial stresses on Path3, which run through lots of weld beads from inner surface to outer surface, are characterized with serrated shape due to steep stress gradient exist in each single weld bead.

6.2 Effect of Local Postwelding Heat Treatment on Residual Stress. Both the ASME VIII and GB 150-2011 recommend that the width of soak band, which defines the width of metal that should be heated above the minimum temperature during local PWHT, should be 1 time the shell thickness or 50 mm on each side of the weld, while the PD 5500 and EN 13445 only recommend that the soak band should cover the weld metal and HAZ. As to the size of heated band, ASME VIII and GB 150-2011 do not provide a specific guidance, but the PD 5500 and EN 13445 recommend that the width of heated band should be $5\sqrt{Rt}$ at least for circumferential weld, where "R" is the internal radius and "t" is the thickness.

In this case, the width of heated band for the closure weld is set to be 300 mm, near $0.5\sqrt{Rt}$, close to the soak band size recommended by ASME VIII and GB 150-2011. The stress distribution along Path1, Path2, and Path3 after the local PWHT predicted by FEM is compared to that of as welded in Figs. 16–18, respectively.

It is obvious that the hoop stress and axial stress are more susceptible to the local PWHT than the radial stress, which maintains at a low level nearly zero along all the three paths after the local PWHT similar to as welded.

From Fig. 16, it is clear that the local PWHT significantly reduce the axial and hoop stress at weld joint on outer surface. The maximum hoop stress within the weld metal and HAZ decreases from 690 MPa to 346 MPa, while that of parent metal changes from compressive stress to tensile stress. The axial stress on the outer surface presents negative values range from −451 MPa to −312 MPa over the whole joint and vicinities.

Figure 17 shows that the local PWHT with heated band width of 300 mm does not lower but elevates the stress level on the inner surface, especially at the parent metal adjacent to the weld. The maximum hoop and axial stresses increase to 431 MPa and 444 MPa, respectively.

The discrepancy between the effects of local PWHT on the stress distributions of inner surface and outer surface can be directly perceived through Fig. 18, which shows the stress

distribution along Path3. It is obviously that the increment of axial stress on inner surface after PWHT is much higher than that of hoop stress. Both the axial stress and hoop stress reach their maximum values on Path3 at the same location about 9–10 mm away from the inner surface. From this location to the outer surface, the hoop stress smoothly decreases from maximum value of 467 MPa to 318 MPa, while the axial stress declines more sharply from 449 MPa to −350 MPa within the rest thickness. Furthermore, quite different from the hoop stress after local PWHT, which maintains tensile stress throughout the whole wall and is about 150–300 MPa lower than as welded within the rest 90% wall thickness, the axial stress after local PWHT translates from tensile stress to compressive stress at the middle of thickness and is higher than as welded within 60% thickness from inner surface, as shown in Fig. 18. From distribution figure of axial stress along Path3, it is easy to speculate that there is bending moment exist in the weld joint caused by local PWHT, which can be validated by the changing of stresses and radial displacements at weld center during the local PWHT, as shown in Fig. 19. Figure 19 shows that the radial displacement at weld center on the inner surface and outer surface are −1.57 mm at the beginning of local PWHT (or as welded), and reach their maximum values of more than 16 mm at the end of holding stage, and eventually reduced to −3.08 mm when the PWHT is completed. At the end of holding stage, all the stresses on both surfaces are nearly zero. When the temperature decreases, hoop stresses on both surfaces increase simultaneously due to circumferential shrinking of the joint. At the same time, the bending moment induced by the radial shrinking of joint inevitably leads to axial compressive stress on the outer surface and detrimental tensile stress on the inner surface, as shown in Fig. 19.

For the purpose of studying the influence of temperature gradient during PWHT, simulations of local PWHT with heated band width of 300 mm on both surfaces and furnace-based uniform PWHT were carried out; the former eliminate radial temperature gradient at weld joint, while the latter one prevents both radial and axial temperature gradient. Figures 20 and 21 diagram the evolutions of stresses and radial displacements at center of weld on both surfaces during these two kinds of heat treatments, respectively. Compared to Fig. 19, it is easily seen that at the end of holding stage, the stresses of all these three types of PWHT are of the same level. However, as the cylinder cooling down, although the uniform PWHT presents the largest thermal deformation, the residual stresses keep at low level due to absence of temperature gradient, as shown in Fig. 20. Figure 21 shows that in the case of heat from both surfaces by 300 mm heated bands, the hoop stress on the outer surface is relative lower than that of heat from outside due to absence of radial temperature gradient in weld joint, but the axial stress on the inner surface increases significantly due to larger bending moment caused by the recovery of larger local
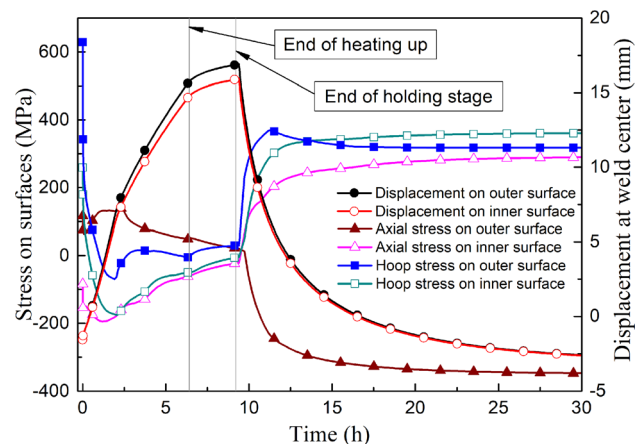
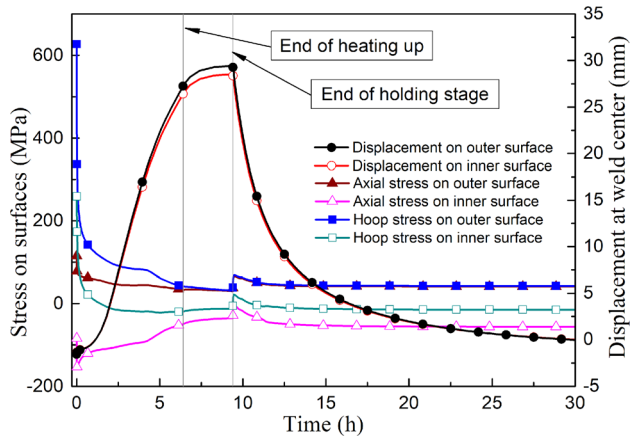**Fig. 19 Evolutions of stresses and displacements at center of weld on surface while heat from outside**

Fig. 20 Evolutions of stresses and displacements at center of weld on surface during uniform PWHT
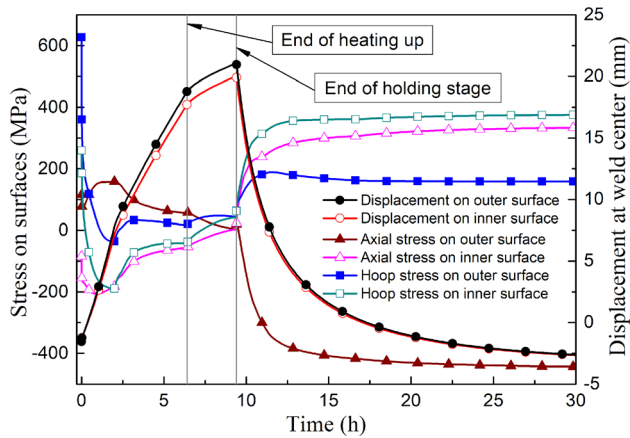

Fig. 21 Evolutions of stresses and displacements at center of weld on surface while heat from both surfaces

thermal deformation. The local deformation is incurred by the harmful axial temperature gradient due to the large heat input at local region. These results indicate that compared to the radial temperature gradient in weld joint induced by the local PWHT, more attention should be focused on reducing axial temperature gradient during the local PWHT. Extending the width of heated band is an effective measure to reduce the axial temperature gradient [30].

6.3 Optimum Size of Heated Band. As discussed earlier, the local PWHT with heated band width of 300 mm significantly reduces the stresses on outer surface of weld joint, but elevates the stress level of inner surface, which must be avoided from viewpoint of reducing the risk of SCC. In order to find out the optimum size of heated band, FE analyses with heated band width range from 100 mm to 3000 mm were conducted to study the effect of heated band size on stress distributions.

Figure 22 represents relations between the maximum values of residual stress on the surface and the size of heated band. It is clear that the stresses on the both surfaces change nonmonotonically with the size of heated band. The axial and hoop stresses on the outer surface reach the minimum value at a certain size of heated band. On the contrast, the stresses on the inner surface have a maximum value at certain size of heated band less than $1\sqrt{Rt}$. Furthermore, it is easy to find that the trend of axial stresses on the inner surface is opposite with that on the outer surface due to the bending moment caused by local PWHT.

From the viewpoint of lower the stress level on inner surface, it is easy to draw a conclusion that the heated band width should not
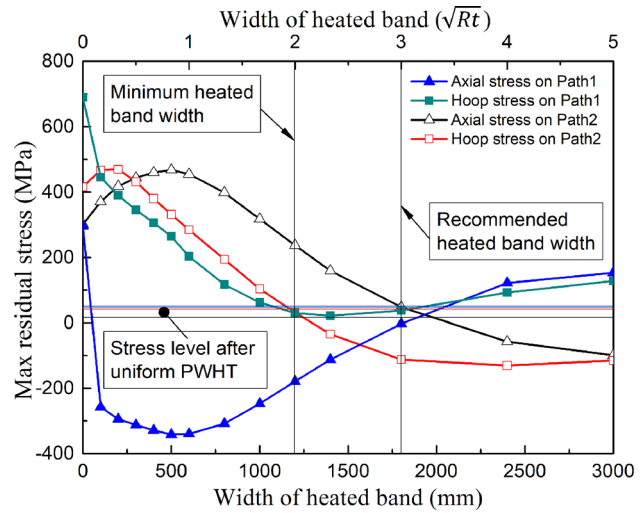

Fig. 22 Relation between the maximum stresses along Path1 and Path2 and the heated band width

be less than $2\sqrt{Rt}$, near 1200 mm in this paper; otherwise, the axial stress on inner surface after local PWHT will be greater than that of as welded. Although the stresses on the inner surface will continue to decrease with the increasing of heated band width, it is worthy to note that the stresses on the outer surface increase simultaneously. In the case studied in this paper, it suggests that the optimum size of heated band is around $3\sqrt{Rt}$ (near 1800 mm). As shown in Fig. 22, as the heated band width is $3\sqrt{Rt}$, the hoop stresses on both surfaces are close to their minimum values, while the axial stresses are reduced to almost zero, and more importantly, stress levels on both surfaces are lower or close to that of uniform PWHT.

7 Conclusions

(1) A generalized plane strain 2D FE model was developed to predict the residual stress distribution of butted weld joint on huge cylinder with ultra-thick wall. The plastic behavior of material under cycle load was taken into account via mixed isotropic–kinematic hardening model. The 3D double-ellipsoid moving heat source was incorporated into the FE model and calibrated by fitting the predicted fusion zone with the macrograph of weld joint. The residual stresses predicted by FE simulation agree well with the results of XRD measurements.

(2) Local PWHT simulation was carried out to determine the stress relief on the inner surface of weld joint. The heated band width deployed in local PWHT is set to be 300 mm, according to the recommended soak band width by ASME VIII and GB150-2011. The results of simulation show that the local PWHT effectively reduce the residual stress on outer surface, which is testified by the XRD measurement. On the contrary, the stress on the inner surface is significantly elevated due to the bending moment induced by local PWHT, which will lead to the increasing risk of SCC in vessels.

(3) Investigation was conducted to find out the relation between stress relief and the heated band width of local PWHT via FEM simulations. Results show that the stresses on the outer surface have a minimum value at a certain size of heated band, while the stresses on the inner surface reach a maximum value when the heated band width is less than $1\sqrt{Rt}$. From the viewpoint of lower the stress level on the inner surface, it is suggested that the heated band width should not be less than $2\sqrt{Rt}$. If the stress relief on the outer surface is taken into account too, the optimum size of heated band of local PWHT for is recommended to be around $3\sqrt{Rt}$.

References

[1] James, M. N., 2011, "Residual Stress Influences on Structural Reliability," Eng. Failure. Anal., 18(8), pp. 1909–1920.

[2] Panontin, T. L., and Hill, M. R., 1996, "The Effect of Residual Stresses on Brittle and Ductile Fracture Initiation Predicted by Micromechanical Models," Int. J. Fract., 82(4), pp. 317–333.

[3] Webster, G. A., and Ezeilo, A. N., 2001, "Residual Stress Distributions and Their Influence on Fatigue Lifetimes," Int. J. Fatigue, 23(1), pp. 375–383.

[4] Nguyen, T. N., and Wahab, M. A., 1998, "The Effect of Weld Geometry and Residual Stresses on the Fatigue of Welded Joints Under Combined Loading," J. Mater. Process. Tech., 77(1–3), pp. 201–208.

[5] Boven, G. V., Chen, W., and Rogge, R., 2007, "The Role of Residual Stress in Neutral pH Stress Corrosion Cracking of Pipeline Steels—Part I: Pitting and Cracking Occurrence," Acta Mater., 55(1), pp. 29–42.

[6] Chen, W., Boven, G. V., and Rogge, R., 2007, "The Role of Residual Stress in Neutral pH Stress Corrosion Cracking of Pipeline Steels—Part II: Crack Dormancy," Acta Mater., 55(1), pp. 43–53.

[7] Ueda, Y., and Yamakawa, T., 1971, "Analysis of Thermal Elastic-Plastic Stress and Strain During Welding by Finite Element Method," Jpn. Weld. Soc. Trans., 2(2), pp. 186–196.

[8] Rybicki, E. F., Schmueser, D. W., Stonesifer, R. W., Groom, J. J., and Mishler, H. W., 1978, "A Finite-Element Model for Residual Stresses and Deflections in Girth-Butt Welded Pipes," ASME J Pressure Vessel Technol., 100(3), pp. 256–262.

[9] Ueda, Y., Murakawa, H., Nakacho, K., and Ma, N. X., 1995, "Establishment of Computational Welding Mechanics (Mechanics, Strength & Structural Design)," Trans. JWRI, 24(2), pp. 73–86.

[10] Goldak, J. A., and Akhlaghi, M., 2005, Computational Welding Mechanics, Springer, New York.

[11] Lindgren, L. E., 2007, Computational Welding Mechanics: Thermomechanical and Microstructural Simulations, Woodhead Publishing, Cambridge, UK.

[12] Song, S., Dong, P., and Pei, X., 2015, "A Full-Field Residual Stress Estimation Scheme for Fitness-for-Service Assessment of Pipe Girth Welds—Part I: Identification of Key Parameters," Int. J. Pressure Vessels Piping, 126–127, pp. 58–70.

[13] Song, S., Dong, P., and Pei, X., 2015, "A Full-Field Residual Stress Estimation Scheme for Fitness-for-Service Assessment of Pipe Girth Welds—Part II: A Shell Theory Based Implementation," Int. J. Pressure Vessels Piping, 128, pp. 8–17.

[14] Dong, P., Song, S., and Zhang, J., 2014, "Analysis of Residual Stress Relief Mechanisms in Post-Weld Heat Treatment," Int. J. Pressure Vessels Piping, 122(1), pp. 6–14.

[15] Wang, X., Gong, J., Zhao, Y., Wang, Y., and Ge, Z., 2016, "Numerical Simulation to Study the Effect of Arc Travelling Speed and Welding Sequences on Residual Stresses in Welded Sections of New Ferritic P92 Pipes," High Temp. Mater. Processes, 35(2), pp. 121–128.

[16] Wang, X., Gong, J., Zhao, Y., Wang, Y., and Wang, Y., 2015, "Prediction of Residual Stress Distributions in Welded Sections of P92 Pipes With Small Diameter and Thick Wall Based on 3D Finite Element Simulation," High Temp. Mater. Processes, 34(3), pp. 227–236.

[17] Mitra, A., Prasad, N. S., and Ram, G. D. J., 2016, "Estimation of Residual Stresses in an 800 mm Thick Steel Submerged Arc Weldment," J. Mater. Process. Technol., 229, pp. 181–190.

[18] McEnerney, J. W., and Dong, P., 2000, "Recommended Practices for Local Heating of Welds in Pressure Vessels," WRC Bull., p. 452.

[19] Wang, J., Lu, H., and Murakawa, H., 1998, "Mechanical Behavior in Local Post Weld Heat Treatment (Report I): Visco-Elastic-Plastic Fem Analysis of Local PWHT (Mechanics, Strength & Structure Design)," Trans. JWRI, 27(1), pp. 83–88.

[20] Murakawa, H., Lu, H., and Wang, J., 1998, "Mechanical Behavior in Local Postweld Heat Treatment (Report II): Determination of Critical Heated Band During Local PWHT (Mechanics, Strength & Structure Design)," Trans. JWRI, 27(1), pp. 89–95.

[21] Lu, H., Wang, J., and Murakawa, H., 1999, "Mechanical Behavior in Local Post Weld Heat Treatment (Report IV): Influence of Residual Stress Distribution in Multi-Pass Welding (Mechanics, Strength & Structure Design)," Trans. JWRI, 28(1), pp. 55–60.

[22] Lu, H., Wang, J., and Murakawa, H., 2002, "Heated Band Width Criterion Based on Stress Relief in Local Post Weld Heat Treatment of Concurrent Tubular Joint (Mechanics, Strength & Structure Design)," Trans. JWRI, 31(1), pp. 77–81.

[23] Nie, C., and Dong, P., 2015, "A Thermal Stress Mitigation Technique for Local Postweld Heat Treatment of Welds in Pressure Vessels," ASME J Pressure Vessel Technol., 137(5), p. 051404.

[24] Pan, J., 2000, Practical Handbook of Pressure Vessel Materials—Carbon Steel and Alloy Steel, Chemical Industry Press, Beijing, China.

[25] Goldak, J., Chakravarti, A., and Bibby, M., 1984, "A New Finite Element Model for Welding Heat Sources," Metall. Mater. Trans. B, 15(2), pp. 299–305.

[26] Smith, M. C., and Smith, A. C., 2009, "NeT Bead-on-Plate Round Robin: Comparison of Transient Thermal Predictions and Measurements," Int. J. Pressure Vessels Piping, 86(1), pp. 96–109.

[27] Smith, M. C., Nadri, B., and Smith, A. C., 2009, "Optimisation of Mixed Hardening Material Constitutive Models for Weld Residual Stress Simulation Using the Net Task Group 1 Single Bead on Plate Benchmark Problem," ASME Paper No. PVP2009-77158.

[28] Muránsky, O., Hamelin, C. J., and Smith, M. C., 2012, "The Effect of Plasticity Theory on Predicted Residual Stress Fields in Numerical Weld Analyses," Comput. Mater. Sci., 54(1), pp. 125–134.

[29] Ying, L., and Guo, F., 2012, "Simulation and Validation of Welding Residual Stresses Based on Non-Linear Mixed Hardening Model," Strain, 48(5), pp. 406–414.

[30] Xu, L., Miao, Y., and Jing, H., 2014, "Experimental and Numerical Investigation of Heated Band Width for Local Post Weld Heat Treatment of ASME P92 Steel Pipe," ASME J Pressure Vessel Technol., 136(1), p. 011401.